Journal of Solid State Electrochemistry (2020) 24:1899–1908
https://doi.org/10.1007/s10008-020-04513-5

ORIGINAL PAPER

CuO/NiO_x thin film–based photocathodes for photoelectrochemical water splitting

Hugo L. S. Santos[1] · Patricia G. Corradini[1] · Marcos A. S. Andrade Jr[1] · Lucia Helena Mascaro[1]

Received: 13 December 2019 / Revised: 20 January 2020 / Accepted: 3 February 2020 / Published online: 8 February 2020

Abstract

Copper oxides are considered to be very promising materials for promoting a hydrogen evolution reaction (HER). However, some CuO features, such as the recombination of charge carriers, electron diffusion length, and the chemical stability need to be improved. In this work, NiO_x was studied as co-catalyst to FTO/CuO, and the films were physically characterised by X-ray diffraction (XRD), X-ray photoelectron spectroscopy (XPS), and scanning electron microscopy (SEM). The photoelectrochemical activity and stability toward the HER were evaluated by depositing films on fluorine-tin doped oxide (FTO) substrate. Although, the CuO (− 3.61 eV) and NiO_x (− 1.13 eV) conduction band positions, estimated by UV-Vis diffuse reflectance and the Mott–Schottky measurements, did not allow electronic transfer from CuO to NiO_x, the formation of a thin layer of NiO_x on CuO was beneficial for the activity of this material. The best CuO/NiO_x film exhibited a photocurrent density of − 1.02 mA cm^{-2} at 0 V vs. RHE, which was higher than that for CuO (− 0.92 mA cm^{-2}). A mechanism of electron transfer between CuO and NiO_x is proposed. The absorption of visible light by CuO leads to the generation of electron-hole pair. Part of the photogenerated electrons are trapped by the NiOOH present in the NiO_x layer, as demonstrated by XPS. The oxy-hydroxide is reduced to metallic Ni, and this species acts as a catalyst for the hydrogen evolution reaction. Due to the increase in interfacial pH caused by the evolution reaction of H_2, the formed metallic Ni can be regenerated to NiO_x.

Keywords Transition metal oxides · *p*-type semiconductor · CuO film · NiO_x film · Water splitting

Introduction

Water splitting has been reported in-depth in the literature, due to its importance in the storage of "energy" in fuel, reducing the seasonality effects inherent in renewable sources. The hydrogen gas obtained in this reaction is considered a sustainable fuel. It can be produced by using the abundant solar energy [1, 2]. This reaction is an attractive alternative because combustion for heat production or for oxidation in fuel cell systems produces water as a byproduct.

A wide variety of photoelectrocatalyst materials, such as metal oxides, sulphides, and non-metallic nitrides, have been investigated for this application and analysed for their efficiency [3–6]. The main goal of these efforts is to design photoelectrochemical cells (PEC) that can conduct, unassisted, both hydrogen evolution and water oxidation reactions [4]. PEC also require semiconductor materials that are able to support charge transfer at a semiconductor/aqueous interface, have long-term stability, and are efficient over the solar spectrum [7]. In addition, the water splitting reaction is sensitive to structure, in which physical characteristics such as morphology and microstructural defects play an important role [8]. Few semiconductor materials meet the requirements for electrode stability in electrolytes to simultaneously reduce and oxidise water [9].

Copper oxides, CuO and Cu_2O, are considered to be very promising materials due to the narrow gap, 1.40 eV and 2.0 eV, respectively, and the conduction band position that allows the hydrogen evolution reaction (HER) [10]. Copper oxides also present interesting features for large scale applications. They are abundantly available, non-expensive, and non-

Electronic supplementary material The online version of this article (https://doi.org/10.1007/s10008-020-04513-5) contains supplementary material, which is available to authorized users.

✉ Lucia Helena Mascaro
lmascaro@ufscar.br

[1] Department of Chemistry, Federal University of São Carlos, Rod. Washington Luiz, Km 235, CEP, São Carlos, São Paulo 13565-905, Brazil

toxic [11]. In terms of photocurrent, Cu_2O can achieve a maximum theoretical photocurrent of 15 mA cm^{-2} under the global standard spectrum (AM1.5 g) of radiation, while CuO can theoretically reach 35 mA cm^{-2} under the same conditions [12, 13]. Although copper oxides have been excellent candidates as photocathodes for HER, they have a high recombination of charge carriers [14], a short electron diffusion length (10–100 nm) [15], and a low chemical stability under the reaction conditions of PEC because they are easily converted to metallic copper in the potentials where water electrolysis occurs [14, 16, 17].

To improve the performance of copper oxides, other materials have been investigated to be used as heterojunctions, or protective or co-catalysed layers. For example, nickel oxides have been shown to be effective co-catalysts for solar-driven H_2 generation [15]. NiO is a *p*-type semiconductor, which shows a high mobility and concentration of photo-induced holes [18]. The interaction between different oxide materials with matching band potentials, such as CuO and NiO, can result in an improvement in the charge separation efficiency and charge carrier lifetimes, and decrease the charge transfer recombination [19].

This work analyses the influence of a NiO_x thin film on the photoelectroactivity of CuO-based photoelectrodes for water splitting, especially for HER. The electrodeposited films were characterised by X-ray diffraction (XRD), X-ray photoelectron spectroscopy (XPS), and scanning electron microscopy (SEM), and photo-electrochemical evaluations were carried out regarding the activity and stability for the HER.

Materials and methods

Preparation of the CuO/NiO_x electrodes

The chemicals were $CuSO_4.5\ H_2O$ (99%, Alfa Aesar), $Ni(NO_3)_2.6\ H_2O$ (99%, Sigma-Aldrich), $C_3H_6O_3$ (lactic acid, 75%, Dinâmica), and Na_2SO_4 (99%, Sigma-Aldrich). The films were electrochemically deposited on F-doped SnO_2 coated glass (FTO) substrates to form the work electrode. A Pt plate was used as counter electrode, and the reference electrode was $Ag_{(s)}|AgCl_{(s)}|Cl^-$ (KCl saturated). The Cu_2O films were electrodeposited following the method described by Golden et al. [20]. The deposition bath was prepared with 0.4 mol L^{-1} $CuSO_4$ and 3.0 mol L^{-1} lactic acid solution at pH 12, adjusted with NaOH. The deposition potential was − 0.45 V, with a charge density cut-off of − 400 mC cm^{-2}. The solution temperature was kept constant at 60 °C. The Cu_2O films were heat treated at 400 °C for 4 h under air atmosphere to obtain the CuO films.

On the CuO prepared films, a thin layer of $Ni(OH)_2$ was deposited. The $Ni(OH)_2$ potential deposition was − 0.7 V, in a bath of 0.02 mol L^{-1} $Ni(NO_3)_2$ solution at pH 6.7 and 25 °C. Three different deposition charge densities were used to obtain the $Ni(OH)_2$ films, i.e. − 20, − 50, and − 100 mC cm^{-2}. The CuO/$Ni(OH)_2$ films were heat treated at 400 °C for 1 h to obtain the CuO/NiO_x films.

Physical and optoelectronic measurements

SEM images were acquired with a high-resolution field emission using a FEG-SEM ZEISS SUPRA 35. The crystalline and morphological features were investigated by XRD using the X-ray diffraction Rigaku DMax-2500 PC (Cu Kα, 1.5406 Å, 40 kV, 2° min^{-1}). XPS measurements were carried out on spectrometer Scienta Omicron, model ESCA 2SR. A Mg Ka monochromator was used to provide the incident photon energy, calibrated using the C 1 s peak (284.8 eV). The optoelectronic characterisation was performed in a NIR-UV-VIS (Varian, CARY 5G) spectrophotometer equipped with a diffuse reflectance module.

Photoelectrochemical and electrochemical impedance spectroscopy characterisations

A quartz window cell was used for the photoelectrochemical reactions. The optical path between the window and the film surfaces was 1 cm in length. The electrochemical measurements were carried-out using a potentiostat/galvanostat (Autolab, MPGSTAT 302N). A solar simulator LCS-100 (Oriel, Newport) equipped with a 100 W Xe lamp was used as a light source. All the experiments were performed using simulated sunlight (100 mW cm^{-2}) and filter AM1.5. The photocurrents from all films were measured in a solution of 0.5 mol L^{-1} Na_2SO_4 adjusted to pH 6. The measurements were carried out by linear sweep voltammetry (LSV) and chronoamperometry (transient photocurrent) under chopped-light.

Electrochemical impedance spectroscopy (EIS) measurements were carried out in the dark for CuO at the potential range of 0.90 to 0.58 V vs. reversible hydrogen electrode (RHE) and for NiO_x (deposited on FTO) at the potential range of 1.0 to 0.8 V vs. RHE, in the optimised frequency of 100 Hz with an AC perturbation amplitude of 10 mV in a solution of 0.5 mol L^{-1} Na_2SO_4 adjusted to pH 6. From the EIS measurements, the charge space capacitances (C_{sc}) of CuO and NiO_x were obtained. A Mott–Schottky (MS) plot was constructed by plotting C_{sc}^{-2} vs. applied potential range.

Results and discussion

Structure and morphology of the CuO and CuO/NiO_x films

The deposition of CuO and CuO/NiO_x films was successful. SEM surface images for the CuO and CuO/NiO_x films are

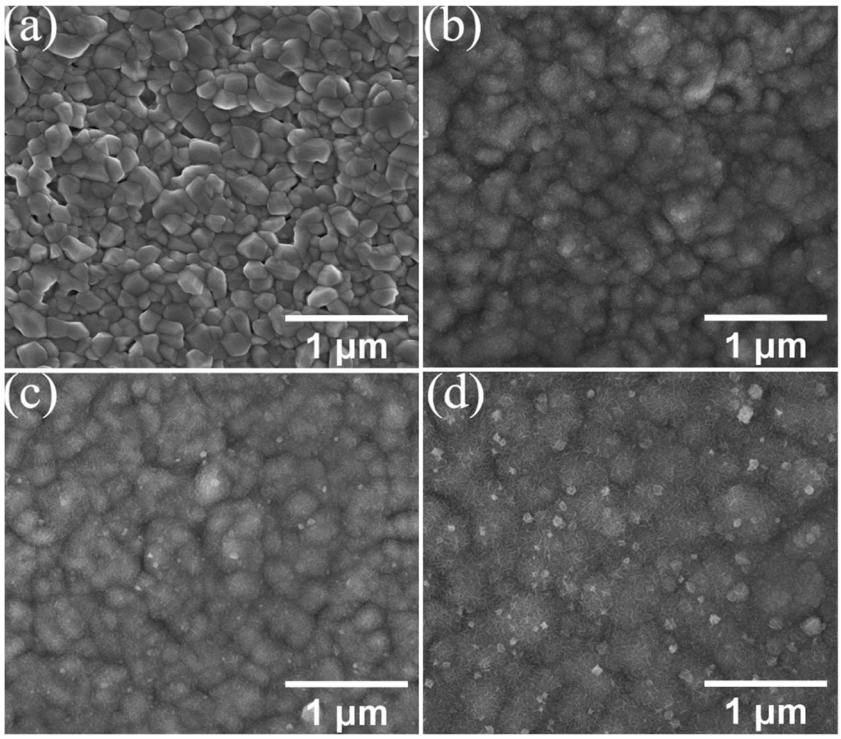

Fig. 1 SEM surface images for films of (**a**) CuO, (**b**) CuO/NiO_x – 20 mC cm^{-2}, (**c**) CuO/NiO_x – 50 mC cm^{-2}, and (**d**) CuO/NiO_x – 100 mC cm^{-2}

shown in Fig. 1. The surface of the CuO film is compact with round shaped grains of different sizes, similar to those reported in the literature [21]. For the films deposited with a charge density of – 20 mC cm^{-2}, it is noted that a thin NiO film covers the grains of CuO, which consequently become less evident with increasing charge (Fig. 1b). As the NiO deposition charge increased to − 50 and – 100 mC cm^{-2} (Fig. 1c and Fig. 1d, respectively), the layer that formed over the CuO film makes it impossible to observe the CuO granular forms. Also, for the CuO/NiO_x 50 and 100, small crystals and structures known as nano-flakes are observed, which are characteristic structures for nickel oxide electrodeposition [22–25].

Figure 2 shows the cross-sectional images for the CuO/NiO_x films. For the CuO/NiO_x compositions, the CuO layers present a compact structure, with similar thicknesses, ranging from 565 to 585 nm. The NiO_x layers became thicker with increasing deposition charge, and the film thicknesses range from 100 to 155 nm from lowest to highest deposition charge density, respectively. These values corroborate with the XRD spectra, given the lack of NiO_x peaks due to the thinness of these films.

Figure 3 shows the XRD patterns for the CuO and CuO/NiO_x films. The diffractograms for all the films present the main characteristic peaks of monoclinic CuO, indexed according to the standard powder diffraction file (PDF) card n° 48–1548 [26, 27]. No characteristic NiO_x peaks is identified, even in films with a high deposition charge density. The lack of NiO peaks may be due to the thinness or low crystallinity of these films. On the other hand, the appearance of the narrow and intense CuO peaks indicates that these films have a high crystallinity. Table 1 shows the average crystallite sizes estimated using the Debye–Scherrer equation [28], on the peak at

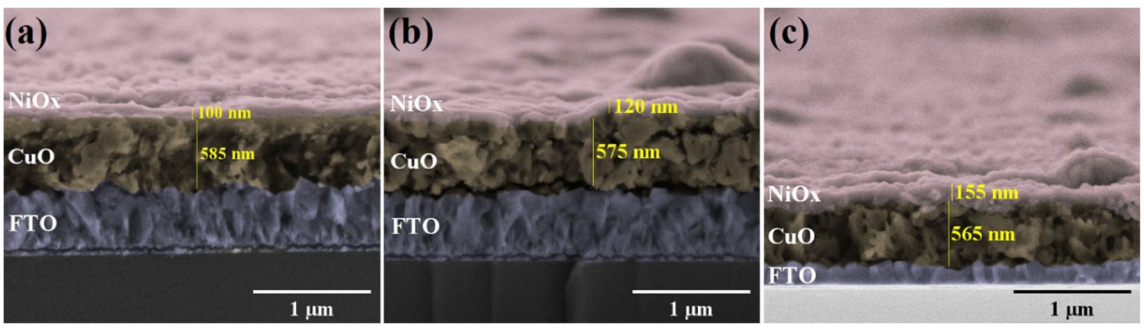

Fig. 2 SEM cross-sectional images for the films of (**a**) CuO/NiO_x – 20 mC cm^{-2}, (**b**) CuO/NiO_x – 50 mC cm^{-2}, and (**c**) CuO/NiO_x – 100 mC cm^{-2}

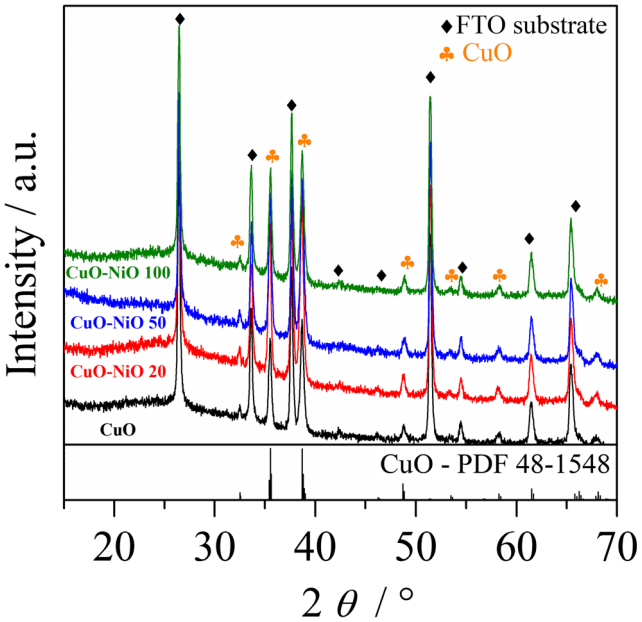

Fig. 3 XRD diffractograms for the CuO and CuO/NiO_x films, with different charge density deposition for the NiO_x films (20, − 20 mC cm^{-2}; 50, − 50 mC cm^{-2}; and 100, − 100 mC cm^{-2})

38.7°. Both the CuO and CuO/NiO materials showed similar crystallite sizes, approximately 22 nm. The NiO_x deposition does not promote changes in the crystallite size. The electrodeposition method promotes crystallite sizes that are higher than those obtained via chemical routes, where the crystallite sizes are 9–16 nm [19, 21]; however, they are smaller than the sizes achieved using the hydrothermal method, where the crystallite size can reach 34 nm [27].

XPS analysis was performed to confirm the superficial species on the CuO/NiO_x films. Figure 4 shows the Cu 2*p* and Ni 2*p* XPS regions of CuO/NiO_x – 50 mC cm^{-2} film. In the Cu $2p_{3/2}$ region (Fig. 4a), the peak located at 934.7 eV is related to Cu(II), and therefore to CuO. Satellite peaks at ~ 942 eV and ~ 960 eV also confirm the presence of Cu(II) [29], and peaks related to metallic copper or Cu(I) are not detected. Two species are detected in the Ni $2p_{3/2}$ region (Fig. 4b), i.e. NiO (855.4 eV) and NiOOH (856.7 eV) [30]. The peaks at 861.8 eV and 879.3 eV refer to satellites [31].

Table 1 Average crystallite size estimated by XRD spectra and bandgap of CuO, and CuO/NiO_x films obtained at different charge densities for NiO_x deposition

Material	Crystallite size (nm)	Bandgap (eV)
CuO	22.2	1.41
CuO/NiO_x 20	23.3	1.44
CuO/NiO_x 50	21.6	1.48
CuO/NiO_x 100	22.4	1.45

The reflectance spectra of all the prepared films are shown in Fig. 5a. The absorption edges around 800 nm indicate that the films have good crystallinity [32]. The CuO/NiO_x films have a lower reflectance when compared with the CuO films. The Kubelka–Munk plots for these materials are presented in Fig. 5b. According to the literature, CuO is a semiconductor that allows indirect electronic transitions between the condition and valence bands, therefore to estimate its bandgap, the Tauc plot is plotted as $(\alpha hv)^{0.5}$ vs. hv [33]. The extrapolation of the linear region can be used to estimate the bandgap energies (E_g), presented in Table 1. The NiO_x deposition does not significantly affect the CuO bandgap; the CuO/NiO_x films have E_g near 1.5 eV, while pure CuO film presents an E_g of 1.4 eV. These E_g values are similar to those reported in the literature, 1.44–1.89 eV [32, 33]. The bandgaps of the films are suitable for absorbing the visible range of the solar spectrum, and they are appropriate for the application of water splitting using solar illumination.

Photoelectrochemical performance of the CuO and CuO/NiO_x films

The PEC performance of the CuO and CuO/NiO_x films for water splitting was examined by linear sweep voltammetry as shown in Fig. 6. The potential originally measured vs. Ag/AgCl was converted to the RHE scale using the following equation:

$$E_{RHE} = E_{Ag/AgCl} + E^{\circ}_{Ag/AgCl} + (0.059 \times pH) \quad (1)$$

where E_{RHE} is the potential in RHE scale, $E_{Ag/AgCl}$ is the potential vs. Ag/AgCl reference electrode experimentally measured, and $E^{\circ}_{Ag/AgCl}$ is the standard potential for Ag/AgCl/sat. KCl (0.197 V) and the pH of the electrolyte is 6.

The photocurrent density was calculated by subtracting the current density measured in the absence of illumination from the photocurrent density measured under illumination. The photocurrent density obtained using CuO films during HER is − 0.92 mA cm^{-2} at 0 V vs. RHE (black line, Fig. 6a). This photocurrent is higher or similar to the photocurrent density of recent works that report bare CuO with planar architecture as a photocathode for water splitting [13, 34–36]. Producing the CuO films by electrodeposition following by annealing enabled the production of high crystallinity and compact CuO thin films. These structural features were beneficial for the hydrogen evolution reaction.

In order to improve the performance of the CuO photocathode, NiO_x co-catalyst thin films were deposited on CuO films. As can be seen in Fig. 6a, the thin NiO_x layers positively affect the CuO film photoelectrochemical behaviour. The CuO/NiO_x 20 film (Fig. 6a, red line), obtained with the lowest NiO_x deposition charge (20 mC cm^{-2}), presents a photocurrent of

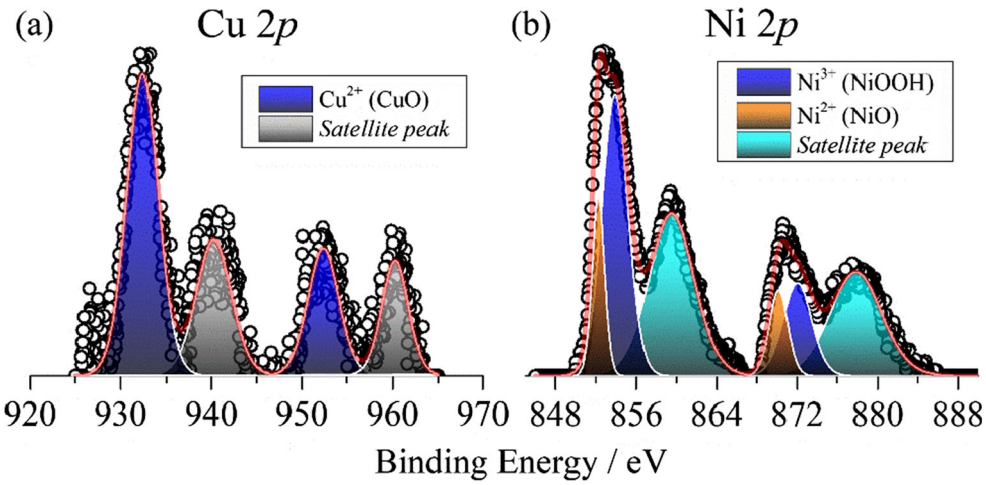

Fig. 4 XPS spectrum for the CuO/NiO_x − 50 mC cm^{-2} film in the (**a**) Cu 2*p* and (**b**) Ni 2*p* regions

− 0.98 mA cm^{-2} at 0 V vs. RHE, higher than that for CuO (− 0.92 mA cm^{-2}). The highest photocurrent was achieved (−1.02 mA cm^{-2}, at 0 V vs. RHE) with the CuO/NiO_x 50 film (Fig. 6a, blue line). The CuO/NiO_x 100 film (Fig. 6a, green line), obtained with the highest NiO_x deposition charge (− 100 mC cm^{-2}), showed a slight decrease of photocurrent, reaching a value of only − 0.90 mA cm^{-2} at 0 V vs. RHE. The decrease in performance of this photoelectrode compared with the others studied here may be related to the internal porosity of the CuO layer or due to the thicker NiO_x layer as shown in Fig. 4c. To obtain the NiO_x layer in the CuO/NiO_x 100 photoelectrode, the CuO film was initially exposed to a potential of − 0.7 V, which is the $Ni(OH)_2$ deposition potential, for a longer time than the other CuO/NiO_x films. On this potential, CuO can be electrochemically converted to Cu_2O or metallic copper [37]. It is suggested that prolonged exposure to potential deposition generates structural modifications, leading to an increase in the internal porosity of the copper oxide layer. Structural defects may result in ohmic contact losses, leading to the inhibition of electron transfer. In addition, these structural defects act as sites of non-radiative recombination [38]. Another factor that maybe negatively influenced the CuO/NiO_x 100 activity is that NiO_x has poor conductivity [39], and a thicker layer of NiO_x can lead to a reduced electronic transfer rate.

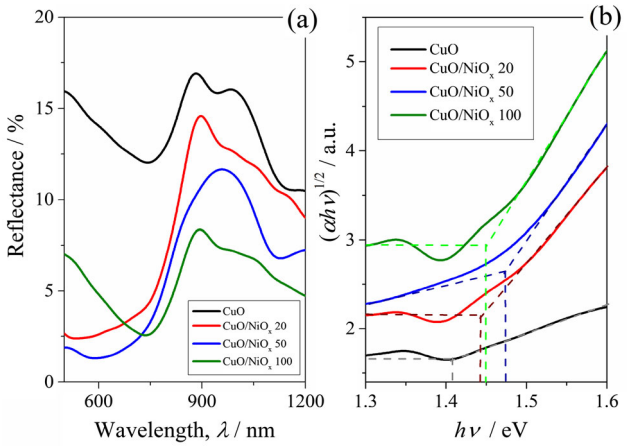

Fig. 5 **a** Diffuse reflectance UV-Vis spectra for the CuO and CuO/NiO_x films. **b** Kubelka–Munk plots for the CuO and CuO/NiO_x films

Although CuO/NiO_x 20 does not present the highest photocurrent, this film is the most stable among the photocathodes studied, as seen in the photocurrent transient shown in Fig. 6b. Despite the fact that CuO/NiO_x 50 has a thicker NiO layer, its photocurrent decreases to half of the initial value by approximately 200 s, similar to pure CuO film. The rapid photodegradation of uncovered CuO is mainly attributed to the competitive photoelectrochemical reduction of CuO to Cu_2O and metallic Cu, which occurs before the thermodynamic potential for water reduction (0 V vs. RHE) [16]. This same behaviour is also seen for the CuO/NiO_x 100 film. As discussed above, the low stability of CuO/NiO_x 50 and CuO/NiO_x 100 are related to the increased internal porosity of the CuO layer due to the long NiO_x deposition time for these films. The internal structural defects in CuO/NiO_x films can act as trappings for the photogenerated electrons, causing them to be used to reduce CuO rather than acting on the photoelectrochemical water splitting [38]. Figure 6c shows the average current density obtained at the different photocurrent transient tests at 0 V vs. RHE of all films. The current densities presented by CuO/NiO_x 20 and CuO/NiO_x 50 films are close, but the increase of NiO_x charge deposition decreased the electrolytic activity of the material, since CuO/NiO_x 100 presents lower values than bare CuO film.

The current spikes observed for CuO and CuO/NiO_x photocurrent transients, when the system is illuminated (Fig. 6b), referee the charge separation in the semiconductors. A *D* parameter was obtained from the photocurrent transient curves shown in Fig. 6b according Eq. 2:

$$D = \frac{j_t - j_{st}}{j_{in} - j_{st}} \quad (2)$$

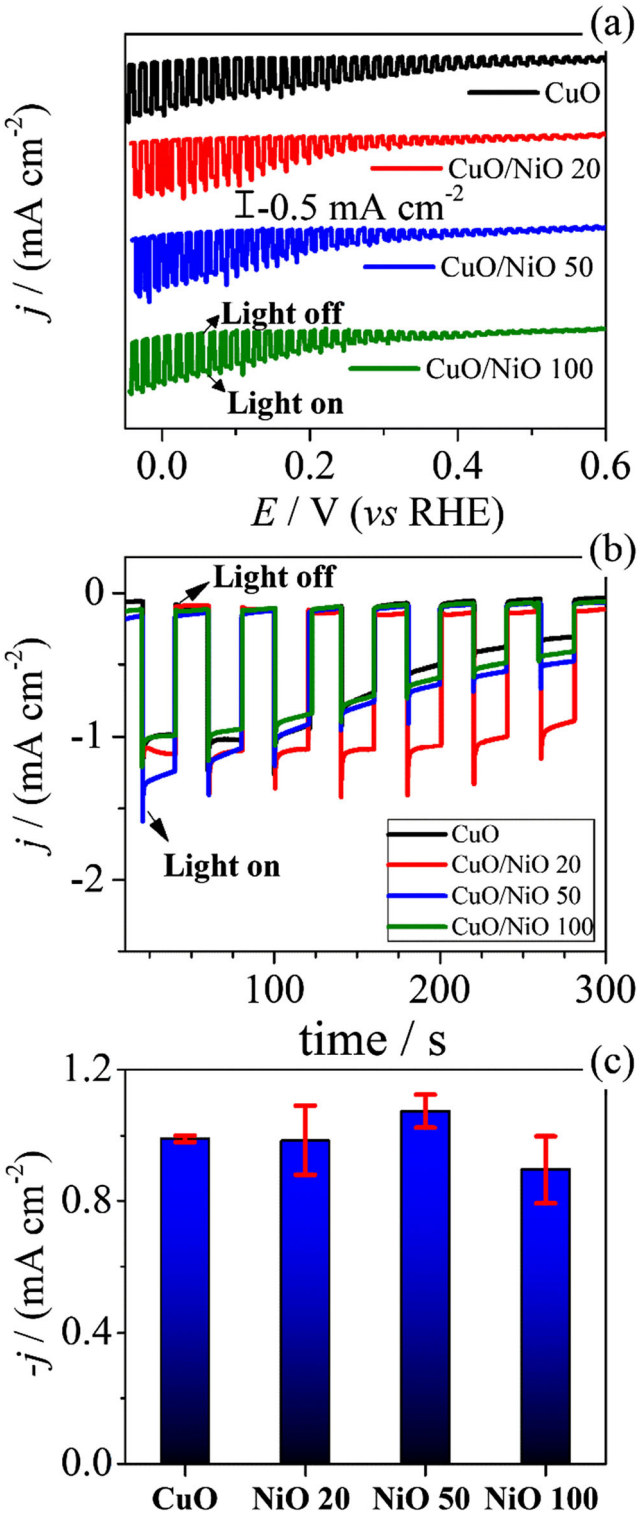

Fig. 6 **a** Linear sweep voltammetry of CuO and CuO/NiO_x films under chopped light (100 mW/cm^{-2} AM 1.5, 5 mV s^{-1}). **b** Photocurrent transient of CuO and CuO/NiO_x films at 0 V vs. RHE. All measurements were carried out in 0.5 mol L^{-1} Na_2SO_4 solution at pH 6. **c** Average current density obtained at the different photocurrent transient tests at 0 V vs. RHE of all films

where j_t is the time-dependent photocurrent density, j_{in} is the initial-time photocurrent density under illumination, and j_{st} is the steady-state photocurrent. The Figure S1a (available in Supplementary Information -SI) illustrates all variables. According to the literature [40–42], the decreasing of j_{in} to j_{st} indicates a recombination process of the photogenerated

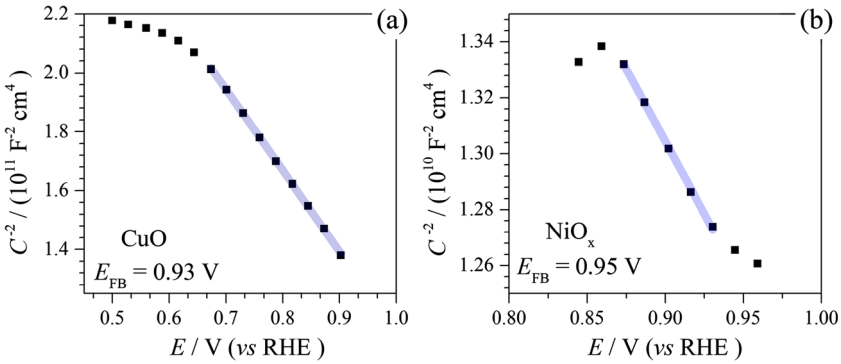

Fig. 7 Mott–Schottky plot of (**a**) bare CuO and (**b**) NiO_x (20 mC cm^{-2}, deposited on FTO)

electron–hole pair. Plot of ln *D* versus time for CuO and CuO/NiO_x films is shown in Figure S1b. A parameter of the recombination of the photogenerated charge carriers kinetic, called as the transient time constant (τ), is defined as the time at ln $D = -1$ (indicated at Fig. S2b). The τ value for CuO, CuO/NiO_x 20, CuO/NiO_x 50, and CuO/NiO_x 100 was estimated to 0.30, 0.67, 0.59, and 0.50 s, respectively. The high values of τ for all CuO/NiO_x films compared with CuO indicate that the layer of NiO_x decreased the charge recombination of CuO film, resulting at a faster charge transfer for the CuO/NiO_x films.

In order to evaluate the electronic structure and to propose a reaction mechanism of the PEC for the photocathodes studied here, EIS measurements for CuO and NiO_x (deposited on FTO) were performed. From the space charge capacitances obtained by EIS at different applied potentials, a MS graph was constructed and the flat band potential (E_{FB}) and the density of majority carriers (N_A) were determined by applying Eq. 3 [16]:

$$\frac{1}{C_{cs}^2} = \frac{2}{e\varepsilon_r\varepsilon_0 N_A A^2}\left(E - E_{fb} - \frac{\kappa_B T}{e}\right) \quad (3)$$

where C_{cs} is the capacitance of the space charge region, *e* is the electron charge, ε_r is the semiconductor dielectric constant, ε_0 is the permittivity of the vacuum, *A* is the electrode area, *E* is the applied potential, $\kappa_B$is the Boltzmann constant, and *T* is the temperature.

The MS graphs for CuO and NiO_x (deposited on FTO, 20 mC cm^{-2}) are shown in Fig. 7. The negative slopes in the linear region of the MS graph for CuO and NiO_x indicate that both semiconductors are *p*-type. The N_A value calculated for CuO is 5.0×10^{19} cm^{-2}, and for NiO_x it is 1.1×10^{21} cm^{-2}, where the dielectric constants are assumed to be 10.26 and 11.9, respectively [43, 44]. The high N_A values for CuO and NiO_x indicate a large amount of Cu and Ni vacancies in the respective semiconductors. Extrapolation of the linear region of the MS graph to the *x*-axis for *p*-type semiconductors gives the E_{FB}. The E_{FB} for CuO and NiO_x is 0.93 and 0.95 V, respectively. The E_{FB} value for both semiconductors should be very close to the valence band potential, given that they have high acceptor densities [16].

Considering the CuO bandgap estimated by UV-Vis diffuse reflectance (1.41 eV, Table 1), the valence and conduction bands are estimated to be 0.93 V and − 0.48 V vs. RHE (corresponding to − 5.01 and − 3.61 eV vs. vacuum), respectively.

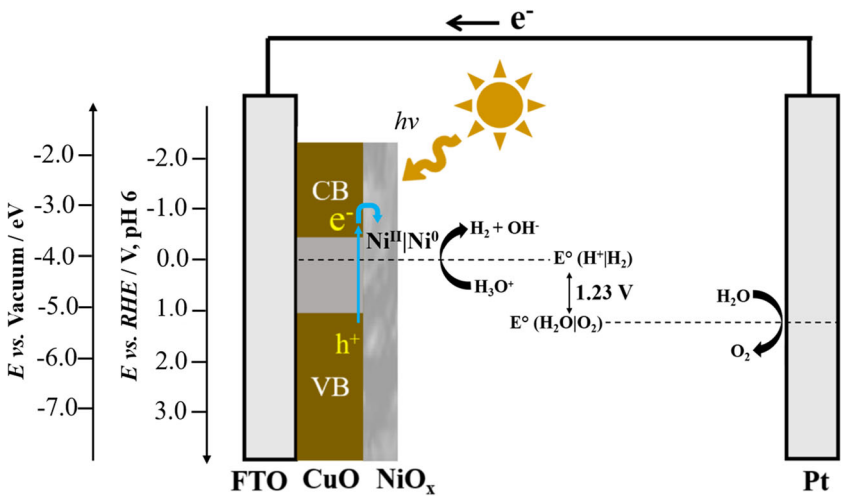

Fig. 8 Schematic illustration of the proposed photo water splitting mechanism on CuO/NiO_x electrodes

For NiO_x, which presents a higher bandgap value (3.9 eV, Fig. S2 in SI), its valence and conduction bands are approximately 0.95 and − 2.95 V vs. RHE (corresponding to − 5.03 and − 1.13 eV vs. vacuum), respectively, similar to those reported in the literature [45]. Analysing the conduction band position of CuO (− 0.48 V vs. RHE) and NiO_x (− 2.95 V vs. RHE), the high negative value of the NiO_x conduction band in relation to CuO does not allow electronic transfer from CuO to NiO_x. However, as shown in the photocurrent curves (Fig. 6), the formation of a thin layer of NiO_x on CuO is beneficial for the activity of this material. $Ni(OH)_2$ and NiO_x have been reported as co-catalysts for photochemical H_2 production on TiO_2 [46] and photoelectrochemical water splitting on Cu_2O [15]. In these reports, nickel oxy-hydroxides act as trapping species of the photogenerated electrons, where they are reduced to metallic Ni, which acts as an active site for H_2 evolution. The CuO conduction band position (− 0.48 V vs. RHE, pH 6) is more negative than TiO_2 (− 0.26 V vs. RHE, pH 6) [46], and the NiO_x layer is mainly composed of NiOOH (Fig. 2), so the electron transfer from CuO to NiO_x should be thermodynamically favourable, as observed in other systems.

Figure 8 illustrates the proposed water splitting mechanism on CuO/NiO_x. The absorption of visible light by CuO leads to the generation of electron-hole pairs. Part of the photogenerated electrons are captured by the oxy-hydroxides present in the NiO_x layer, which reduces to metallic Ni and acts as a catalyst of the hydrogen evolution reaction. Due to the increase in interfacial pH caused by the evolution reaction of H_2, the formed metallic Ni can be regenerated to NiO_x.

As a way to evaluate the stability of CuO and CuO/NiO_x 20 and CuO at longer reaction times, these photocathodes were submitted to photoelectrochemical water splitting at 0 V vs RHE for 40 min. Figure 9 shows that both photocurrent of CuO bare (Fig. 9a) and for CuO/NiO_x 20 (Fig. 9b) are stable during the experiment. However, the linear sweep voltammetry performed after the phototransient curves, at Fig. 9c, shows that CuO/NiO_x 20 presents higher current densities than CuO. This result is observed mainly for potential lower than 0.25 V. The better CuO/NiO_x 20 stability may be related to two factors, i.e. lower physic contact between CuO and the electrolyte provide by NiO_x layer, and facilitated transfer of photogenerated electrons provided by the co-catalyst NiO_x layer.

Conclusion

Herein, we studied NiO_x as co-catalysts to FTO/CuO, by electrodeposition of NiO_x at different deposition charges (− 20, − 50, and − 100 mC cm^{-2}). It was observed in the SEM images that the deposition of NiO_x covered the compact CuO film, and the higher the deposition charge, the thicker the NiO_x layer.

The formation of a thin layer of NiO_x over CuO is beneficial for the activity of this material. The best CuO/NiO_x exhibited a photocurrent density of − 1.02 mA cm^{-2} at 0 V vs. RHE, higher than that for bare CuO (− 0.92 mA cm^{-2}). The CuO (− 3.61 eV) and NiO_x (− 1.13 eV) conduction band positions, estimated by UV-Vis diffuse reflectance and MS measurements, do not allow electronic transfer from CuO to NiO_x. As demonstrated by XPS, the NiO_x layer is mainly composed of NiOOH, and this species acts as scavenger species of the photogenerated electrons, which is reduced to metallic Ni, and acts as an active site for H_2 evolution. Therefore, a mechanism on CuO/NiO_x was proposed. The absorption of visible light by CuO leads to the generation of electron-hole pairs. Part of the photogenerated electrons are sequestered by the oxy-hydroxides present in the NiO_x layer, which reduces to metallic Ni and acts as a catalyst for the hydrogen evolution reaction. Due to the increase in interfacial pH caused by the evolution reaction of H_2, the metallic Ni that is formed can be regenerated to NiO_x.

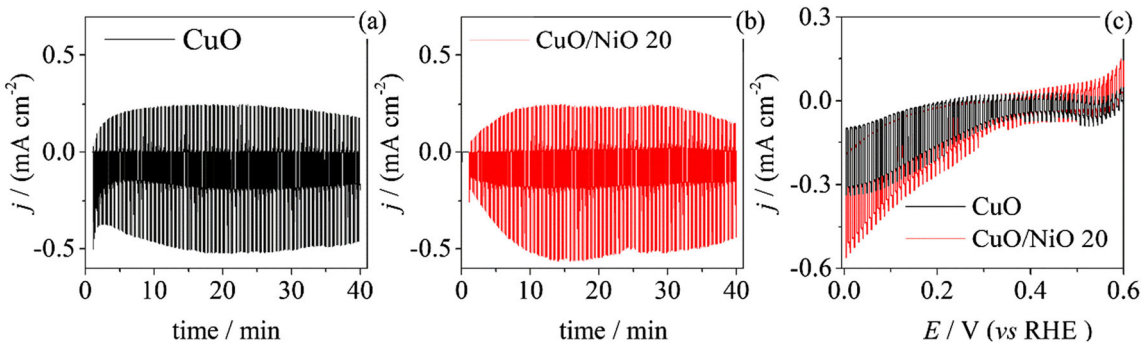

Fig. 9 Photocurrent transient of (**a**) CuO and (**b**) CuO/NiO_x 20 films at 0 V vs. RHE, and (**c**) linear sweep voltammetry of CuO and CuO/NiO_x 20 films after the photocurrent transient tests, under chopped light (100 mW cm^{-2} AM 1.5, 5 mV s^{-1})

Funding information The authors thank the São Paulo Research Foundation (FAPESP) for the financial assistance for the project and for the fellowships that were granted (grant no. 2017/11986-5, grant no. 2018/16401-8, grant no. 2017/12794-2, FAPESP/CDMF #2013/07296-2), and Shell and the strategic importance of the support given by ANP (Brazil's National Oil, Natural Gas and Biofuels Agency) through the R&D levy regulation. The authors also thank the Coordenação de Aperfeiçoamento de Pessoal de Nível Superior (CAPES) - Finance Code 001, and the Conselho Nacional de Pesquisa e Desenvolvimento (CNPq, #141092/2018-1) for the fellowships that were granted.

References

1. Wang JY (2015) Barriers of scaling-up fuel cells: cost, durability and reliability. Energy 80:509–521
2. He H, Liao A, Guo W, Luo W, Zhou Y, Zou Z (2019) State-of-the-art progress in the use of ternary metal oxides as photoelectrode materials for water splitting and organic synthesis. Nano Today 28: 100763
3. Chen X, Shen S, Guo L, Mao SS (2010) Semiconductor-based photocatalytic hydrogen generation. Chem Rev 110(11):6503–6570
4. Walter MG, Warren EL, McKone JR, Boettcher SW, Mi QX, Santori EA, Lewis NS (2010) Solar water splitting cells. Chem Rev 110(11):6446–6473
5. Chen J, Yang D, Song D, Jiang J, Ma A, Hu MZ, Ni C (2015) Recent progress in enhancing solar-to-hydrogen efficiency. J Power Sources 280:649–666
6. Medina M, Corradini PG, Mascaro LH (2019) Facile one-step electrodeposition fabrication of amorphous MoS2 catalysts in titanium for hydrogen evolution reaction. J Braz Chem Soc:1–9
7. Ismail AA, Bahnemann DW (2014) Photochemical splitting of water for hydrogen production by photocatalysis: a review. Sol Energy Mater Sol Cells 128:85–101
8. Pham TA, Ping Y, Galli G (2017) Modelling heterogeneous interfaces for solar water splitting. Nat Mater 16(4):401–408
9. Gupta NM (2017) Factors affecting the efficiency of a water splitting photocatalyst: a perspective. Renew Sust Energ Rev 71:585–601
10. Li J, Cui M, Guo Z, Liu Z, Zhu Z (2014) Synthesis of dumbbell-like CuO–$BiVO_4$ heterogeneous nanostructures with enhanced visible-light photocatalytic activity. Mater Lett 130:36–39
11. Bagal IV, Chodankar NR, Hassan MA, Waseem A, Johar MA, Kim D-H, Ryu S-W (2019) Cu2O as an emerging photocathode for solar water splitting - a status review. Int J Hydrogen Energ 44(39): 21351–21378
12. Paracchino A, Laporte V, Sivula K, Grätzel M, Thimsen E (2011) Highly active oxide photocathode for photoelectrochemical water reduction. Nat Mater 10(6):456–461
13. Masudy-Panah S, Siavash Moakhar R, Chua CS, Tan HR, Wong TI, Chi D, Dalapati GK (2016) Nanocrystal engineering of sputter-grown CuO photocathode for visible-light-driven electrochemical water splitting. ACS Appl Mater Interfaces 8(2):1206–1213
14. Dubale AA, Tamirat AG, Chen H-M, Berhe TA, Pan C-J, Su W-N, Hwang B-J (2016) A highly stable CuS and CuS–Pt modified Cu2O/CuO heterostructure as an efficient photocathode for the hydrogen evolution reaction. J Mater Chem A 4(6):2205–2216
15. Lin C-Y, Lai Y-H, Mersch D, Reisner E (2012) Cu2O|NiOx nanocomposite as an inexpensive photocathode in photoelectrochemical water splitting. Chem Sci 3(12):3482–3487
16. Septina W, Prabhakar RR, Wick R, Moehl T, Tilley SD (2017) Stabilized solar hydrogen production with CuO/CdS heterojunction thin film photocathodes. Chem Mater 29(4):1735–1743
17. Morales-Guio CG, Tilley SD, Vrubel H, Grätzel M, Hu X (2014) Hydrogen evolution from a copper(I) oxide photocathode coated with an amorphous molybdenum sulphide catalyst. Nat Commun 5(1):3059
18. Ren X, Gao P, Kong X, Jiang R, Yang P, Chen Y, Chi Q, Li B (2018) NiO/Ni/TiO2 nanocables with Schottky/p-n heterojunctions and the improved photocatalytic performance in water splitting under visible light. J Colloid Interface Sci 530:1–8
19. Juma AO, Arbab EAA, Muiva CM, Lepodise LM, Mola GT (2017) Synthesis and characterization of CuO-NiO-ZnO mixed metal oxide nanocomposite. J Alloys Compd 723:866–872
20. Golden TD, Shumsky MG, Zhou Y, VanderWerf RA, Van Leeuwen RA, Switzer JA (1996) Electrochemical deposition of copper(I) oxide films. Chem Mater 8(10):2499–2504
21. Dolai S, Sarangi SN, Hussain S, Bhar R, Pal AK (2019) Magnetic properties of nanocrystalline nickel incorporated CuO thin films. J Magn Magn Mater 479:59–66
22. Jagadale AD, Kumbhar VS, Dhawale DS, Lokhande CD (2013) Potentiodynamically deposited nickel oxide (NiO) nanoflakes for pseudocapacitors. J Electroanal Chem 704:90–95
23. Wu M-S, Huang Y-A, Yang C-H (2008) Capacitive behavior of porous nickel oxide/hydroxide electrodes with interconnected nanoflakes synthesized by anodic electrodeposition. J Electrochem Soc 155(11):A798–A805
24. Huang M, Li F, Zhang YX, Li B, Gao X (2014) Hierarchical NiO nanoflake coated CuO flower core–shell nanostructures for supercapacitor. Ceram Int 40(4):5533–5538
25. Xu H, Zhang J, Rehman AU, Gong L, Kan K, Li L, Shi K (2017) Synthesis of NiO@CuO nanocomposite as high-performance gas sensing material for NO2 at room temperature. Appl Surf Sci 412: 230–237
26. Hou L, Zhang C, Li L, Du C, Li X, Kang X-F, Chen W (2018) CO gas sensors based on p-type CuO nanotubes and CuO nanocubes: morphology and surface structure effects on the sensing performance. Talanta 188:41–49
27. Wang W, Bai C, Zhang L (2019) CuO/graphene oxide composite as a highly active catalyst for one-step amination of benzene to aniline. Catal Commun 125:1–5
28. Khorsand Zak A, Majid WHA, Ebrahimizadeh Abrishami M, Yousefi R, Parvizi R (2012) Synthesis, magnetic properties and X-ray analysis of Zn0.97X0.03O nanoparticles (X = Mn, Ni, and co) using Scherrer and size–strain plot methods. Solid State Sci 14(4):488–494
29. Sen B, Kuyuldar E, Şavk A, Calimli H, Duman S, Sen F (2019) Monodisperse rutheniumcopper alloy nanoparticles decorated on reduced graphene oxide for dehydrogenation of DMAB. Int J Hydrogen Energ 44(21):10744–10751
30. Sui L, Yu T, Zhao D, Cheng X, Zhang X, Wang P, Xu Y, Gao S, Zhao H, Gao Y, Huo L (2019) In situ deposited hierarchical CuO/NiO nanowall arrays film sensor with enhanced gas sensing performance to H2S. J Hazard Mater:121570
31. Biesinger MC, Payne BP, Lau LWM, Gerson A, Smart RSC (2009) X-ray photoelectron spectroscopic chemical state quantification of mixed nickel metal, oxide and hydroxide systems. Surf Interface Anal 41(4):324–332
32. Lun T-T, Liu C-Q, Wang N, Zhai X-N, Song M-S, Ge Q, Zhang X-Y, Liu S-M, Wang H-L, Jiang W-W, Ding W-Y (2019) Preparation of compact CuO films by sol-gel spin coating technique. Mater Lett 257:126745
33. Senobari S, Nezamzadeh-Ejhieh A (2018) A comprehensive study on the enhanced photocatalytic activity of CuO-NiO nanoparticles: designing the experiments. J Mol Liq 261:208–217

34. Lim Y-F, Chua CS, Lee CJJ, Chi D (2014) Sol–gel deposited Cu2O and CuO thin films for photocatalytic water splitting. Phys Chem Chem Phys 16(47):25928–25934
35. Emin S, Abdi FF, Fanetti M, Peng W, Smith W, Sivula K, Dam B, Valant M (2014) A novel approach for the preparation of textured CuO thin films from electrodeposited CuCl and CuBr. J Electroanal Chem 717-718:243–249
36. Wang P, Wen X, Amal R, Ng YH (2015) Introducing a protective interlayer of TiO2 in Cu2O–CuO heterojunction thin film as a highly stable visible light photocathode. RSC Adv 5(7):5231–5236
37. Nakayama S, Kaji T, Shibata M, Notoya T, Osakai T (2007) Which is easier to reduce, Cu2O or CuO ? J Electrochem Soc 154(1):C1–C6
38. Cremades A, Piqueras J (2002) Study of carrier recombination at structural defects in InGaN films. Mater Sci Eng B 91-92:341–344
39. Jang W-L, Lu Y-M, Hwang W-S, Chen W-C (2010) Electrical properties of Li-doped NiO films. J Eur Ceram Soc 30(2):503–508
40. Zhang K, Shi X-J, Kim JK, Park JH (2012) Photoelectrochemical cells with tungsten trioxide/Mo-doped BiVO4 bilayers. Phys Chem Chem Phys 14(31):11119–11124
41. Dey KK, Gahlawat S, Ingole PP (2019) BiVO4 optimized to nanoworm morphology for enhanced activity towards photoelectrochemical water splitting. J Mater Chem A 7(37):21207–21221
42. Singh AK, Sarkar D (2019) Enhanced light absorption and charge carrier management in core-shell Fe2O3@nickel nanocone photoanodes for photoelectrochemical water splitting. Chemcatchem 11(24):6355–6363
43. Zhang Z, Wang P (2012) Highly stable copper oxide composite as an effective photocathode for water splitting via a facile electrochemical synthesis strategy. J Mater Chem 22(6):2456–2464
44. Rao KV, Smakula A (1965) Dielectric properties of cobalt oxide, nickel oxide, and their mixed crystals. J Appl Phys 36(6):2031–2038
45. Fingerle M, Tengeler S, Calvet W, Mayer T, Jaegermann W (2018) Water interaction with sputter-deposited nickel oxide on N-Si photoanode: cryo photoelectron spectroscopy on adsorbed water in the frozen electrolyte approach. J Electrochem Soc 165(4):H3148–H3153
46. Yu J, Hai Y, Cheng B (2011) Enhanced photocatalytic H2-production activity of TiO2 by Ni(OH)2 cluster modification. J Phys Chem C 115(11):4953–4958